Superhydrophobic Aluminum Surfaces: Preparation Routes, Properties and Artificial Weathering Impact

M. Thieme [a,*], **C. Blank** [a], **A. Pereira de Oliveira** [b], **H. Worch** [a], **R. Frenzel** [c], **S. Höhne** [c], **F. Simon** [c], **H. G. Pryce Lewis** [d] **and A. J. White** [d]

[a] Technische Universität Dresden (TUD), Institute of Materials Science, D-01062 Dresden, Germany
[b] TUD, now at: Universidade Estadual de Campinas UNICAMP, Faculdade de Engenharia Química, Cidade Universitária "Zeferino Vaz", Av. Albert Einstein 500, Campinas, SP, Brazil
[c] Leibniz Institute of Polymer Research Dresden (IPF), Hohe Str. 6, D-01069 Dresden, Germany
[d] GVD Corporation, 45 Spinelli Place, Cambridge, MA 02138, USA

Abstract

Among the materials that can be treated in order to impart superhydrophobic properties are many originally hydrophilic metals. For this, they must undergo a sequential treatment, including roughening and hydrophobic coating. This contribution presents various preparation routes along with various characterization methods, such as dynamic contact angle (DCA) measurements, scanning electron microscopy (SEM) and spectroscopic techniques (FT–IRRAS, XPS, EIS).

Micro-rough surfaces of pure and alloyed aluminum were generated most easily by using a modifie *S*ulfuric *A*cid *A*nodization under *I*ntensifie conditions (*SAAi*). This produces a micro-mountain-like oxide morphology with peak-to-valley heights of 2 µm and sub-µm roughness components. Additionally, micro-embossed and micro-blasted surfaces were investigated. These micro-roughened initial states were chemically modifie with a solution of a hydrophobic compound, such as the reactive f uoroalkylsilane *PFATES*, the reactive alkyl group containing polymer *POMA*, or the polymer *Teflo* ® AF. Alternatively, the chemical modificatio was made by a *H*ot *F*ilament *C*hemical *V*apor *D*eposition (*HFCVD*) of a *PTFE* layer. The latter can form a considerably higher thickness than the wet-deposited coatings, without detrimental leveling effects being observed in comparison with the original micro-rough surface. The inherent and controllable morphology of the *PTFE* layers represents an important feature. The impacts of a standardized artificia weathering (*WTH*) on the wetting behavior and the surface-chemical properties were studied and discussed in terms of possible damage mechanisms. A very high stability of the superhydrophobicity was observed for the f uorinated wet-deposited *PFATES* and *Teflo* ® AF coatings as well as for some of the *PTFE* layer variants, all on *SAAi*-pretreated substrates. Very good results were also obtained for specimens produced by appropriate mechanical roughening and *PTFE* coating.

---

* To whom correspondence should be addressed. Tel.: 0049 351 463-36461; Fax: 0049 351 463-33207; e-mail: michael.thieme@tu-dresden.de

Keywords
Aluminum, superhydrophobicity, anodic oxidation, micro-embossing, wet-deposited coatings, PTFE layers, artificia weathering

1. Introduction

The phenomenon of superhydrophobicity (SH, earlier designated as ultrahydrophobicity) has received much attention for more than a decade by numerous research groups, extending the crucial and exciting investigations of Barthlott and Neinhuis [1]. SH as define by water contact angles (CA) of more than 150°, a negligible hysteresis (the difference of the advancing and receding CAs, θ_a and θ_r, respectively) and extremely low droplet roll-off angles is based on the interplay of morphological and surface-chemical properties, which lower the surface free energy down to very small values. From the literature it can be seen that the micro-roughness has in most cases more than one lateral/transversal component covering micro- and submicro dimensions [2–4]. Some researchers postulated a fractal character [5]. With regard to the structural properties of superhydrophobic surfaces, the spectrum covers layered structures with self-assembled monolayers (SAMs) of water-repellent compounds to polymer layers of considerable thickness as well as intrinsically hydrophobic polymers with suitable morphology. It has been stated that the surface free energies of molecular groups rank according to $CH_2 > CH_3 > CF_2 > CF_3$ [6]. Fluorine-substituted organic compounds are, therefore, generally preferred for imparting a surface with SH. Moreover, they are characterized by the exceptionally high strength of the C–F bond as well as by high chemical and biological inertness [7]. There are literature surveys that reflec the state-of-the-art of science and technology in the f eld of SH in great details [8–10]. A survey of superhydrophobic aluminum is given elsewhere [11]. Because Al with its native oxide has a hydrophilic character, it must undergo sequential roughening and coating treatment steps in order to obtain superhydrophobic properties.

The far-reaching commercial possibilities of the so-called Lotus-*effect*® are, at present, only being seldom utilized. This is, in part, caused by the use of other advanced technologies for self-cleaning (as with photocatalytically acting superhydrophilic glass [12]). Moreover, a major reason for this is the fact that SH is intimately associated with the uppermost surface layers. Thus, SH is generally sensitive to mechanical impacts, e.g. from handling, as well as from the (photo-)chemical attack, i.e. from weathering.

This contribution looks at novel preparation routes as well as the behavior of superhydrophobic Al material after artificia weathering. The surfaces were prepared by both micro-roughening and chemical modification In addition to our anodization approach using sulfuric acid [13, 14], we present the novel variants of elevated-temperature micro-embossing and micro-blasting as purely mechanical ways for achieving a suitably roughened surface (cf. [11]). Other roughening variants developed [13, 15–17] are not considered here. For the subsequent coating

step, two novel compounds of quite different nature were successfully applied for imparting SH and tested for their weathering behavior: i — the reactive polymer poly(octadecene-*alt*-maleic anhydride) (*POMA*), which can be grafted onto previously deposited chitosan (N-amino-2-desoxy-β-D-glycopyranose, *Chs*), which acts as an anchor and, moreover, which was found to lead to strengthening effects of the anodic oxide [11, 18, 23], and ii — poly(tetrafluoroethylene (*PTFE*), which was deposited by hot filamen chemical vapor deposition (*HFCVD*) [19–21] with various thicknesses and morphologies. Further, perfluoroal ylethyltriethoxysilane (*PFATES*) and [3-(2-aminoethyl) aminopropyl] trimethoxysilane plus *Teflo* ® AF (*AS/TAF*) [13, 15] were compared to these layers.

Mechanical properties of the produced systems as obtained from micro- and nano-hardness measurements as well as from gentle abrasion tests are reported in Ref. [11].

2. Experimental

2.1. Materials and Preparation Methods

2.1.1. Substrate Materials

Sheets ($26 \times 38 \times 1$ mm^3) of Al Mg1 (AA 5005) were the main substrate material, with analytical grade Al 99.95 (Merck) and pure aluminum 99.5 (AA 1050) used for comparison. Using the Brinell hardness test (ISO 6506-1:2005), the following hardness values were determined: 52 HBW 2.5/31.25 for Al Mg1, 35 HBW 2.5/15.625 for Al 99.5. Rod specimens (5 mm in diameter) of Al MgSi0.5 (AA 6060) were used for EIS testing (see below).

2.1.2. Sulfuric Acid Anodization under Intensifie Conditions, SAAi

The electrolyte solution was a mixture of sulfuric acid and aluminum sulfate (starting concentration 0.1 mol/l) with a total sulfate concentration of 2.3 mol/l. The anodization was carried out at (40 ± 1)°C, 30 mA/cm^2 for 1200 s [13, 14]. The conditions of the usual anodization procedure (*SAAu*) were <20°C, 15 mA/cm^2, and 1200 s. The anodization followed an initial etching treatment using 1 mol/l NaOH (600 s) with subsequent neutralizing in 1 mol/l HNO_3 (60 s).

2.1.3. Intermediate Deposition of Chitosan

Chitosan was deposited either by cathodic precipitation from a 1 wt.% solution in 1 vol.% acetic acid, pH = 3.8 at -5 mA/cm^2 for 40 s (*Chs-e*) or by immersion in the same solution for 1800 s (*Chs-i*) [18].

2.1.4. Micro-embossing under Annealing Conditions, ME

The embossing operation was done at 350°C and 120 MPa using a laser-structured SiC tool (stamp diameter 18 mm), having hexagonally arranged cone-shaped holes (spaced at intervals of 23 μm and about 25 μm deep).

2.1.5. Micro-blasting, MB

Corundum powders (grit 600, 800, 1000, 1200) were applied as a fin beam at 6 bar pressure under manual control.

2.1.6. Wet-Chemical Dip Coating Treatments

i — Poly(octadecene-*alt*-maleic anhydride) (*POMA*) was applied as a 0.1 wt.% solution in acetone at ambient temperature for 30 min, followed by a vacuum-drying step. ii — Perfluoroal ylethyltriethoxysilane (*PFATES*) was applied in tert-butyl methyl ether (2 vol.%) for 180 min in the presence of 0.1 vol.% of triethylamine as a catalyst; iii — N-(2-aminoethyl)-3-aminopropyltrimethoxysilane was applied in a 10 vol.% ethanolic solution for 180 min, followed by spin-coating (5000 min^{-1}, 30 s) with a solution of the copolymer *Teflo* ® AF (1 wt.% in FC 75 solvent) (*AS/TAF*). All steps were followed by rinsing and annealing at 120°C for 1 h.

2.1.7. HFCVD

The process consists of thermal decomposition (>150°C) of the precursor hexaflu oropropylene oxide, which is associated with radical formation, and polymerization to *PTFE*. The deposition thicknesses used were 50, 250, 500 and 1000 nm. Besides the standard coating conditions a number of other variants were employed, such as post-deposition annealing, deposition at elevated substrate temperature, and lower pressure conditions during deposition.

2.2. Artificia Weathering

The weathering procedure was carried out in two ways: (i) Normal weathering exposure (*WTH*) for 360 h, comprising of continuous xenon-arc irradiation (filtere corresponding to day-light spectral distribution at a black-standard temperature of 55°C) and a cyclic sequence of shower wetting (18 min) and drying at relative air humidity of 60–80% (102 min), and (ii) special weathering exposure using irradiation, but excluding moisture (*WTH-L*) (Xenotest Alpha; Atlas, Chicago, IL).

2.3. Characterization

2.3.1. Dynamic Contact Angle (DCA) Measurement

DCA measurements were made at f ve different positions on each specimen using a maximum droplet size of 30–50 µl. The contact angle data were averaged from about 20 successive measurements during advancing and receding (DSA 10, Krüss/ Germany).

2.3.2. Scanning Electron Microscopy (SEM)

The images were taken at an acceleration voltage of 2 keV in a DSM 982 Gemini equipment (Zeiss/Germany).

2.3.3. Fourier-Transform Infrared Reflection-Absorptio Spectroscopy (FT–IRRAS)

The spectra were recorded using an FTS 2000 instrument (Perkin-Elmer/Germany) over the frequency range of 550–4000 cm^{-1} as averages of 256 individual spectra

measured at four positions on each sample. The analyzed spot had a diameter of ca. 100 µm.

2.3.4. X-Ray Photoelectron Spectroscopy (XPS)

The analysis utilized monochromatic Al Kα radiation, charge compensation and step widths of 0.3 eV for survey spectra, or 0.02 eV for high-resolution spectra (Axis Ultra, Kratos/UK). The scale was calibrated using the C_{1s} binding energy of saturated hydrocarbons, which was set at 285 eV. The maximum information depth for the C_{1s} peak was about 10 nm [24–26].

2.3.5. Electrochemical Impedance Spectrometry (EIS)

Spectra were recorded in the frequency range of 100 kHz–0.5 mHz using a 0.133 mol/l phosphate buffer test solution pH = 6.0 and an IM 6 instrument (Zahner/Germany). Sheet specimens were tested using an O-ring cell (effective area 0.25 cm^2). Alternatively, rod specimens were used in a three-electrode cell arrangement with a concentric platinum net counter electrode and a Haber–Luggin capillary (cf. [22]). The depth of immersion was 40 mm. The measurements were made at least twice for each of the selected sample states.

3. Results

3.1. Substrate Surfaces

Irrespective of the material employed, the *SAAi* pretreatment leads to a specifi morphology of the oxide layer produced which is characterized by an irregularly ordered mountain-like structure showing typical top-to-valley and lateral distances of about 2 µm each (Fig. 1a). This structure is produced more uniformly on the pure Al as compared to the technical Al substrates. At higher magnification a sub-µm fibre-li e roughness is also observed (Fig. 1b).

In contrast, surfaces treated by the usual *SAAu* method have a more or less f at, rippled morphology (Fig. 1c). For details of layers formation, their structures and compositions see Refs. [13, 14, 22].

Chitosan can be deposited onto anodized aluminum from a diluted acetic acid medium by means of a cathodic process, which causes interfacial alkalization and,

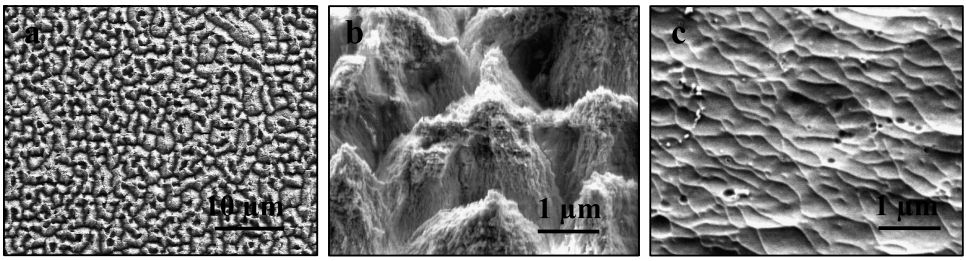

Figure 1. SEM images of different anodized surfaces; (a) *SAAi*-treated Al 99.95; (b) *SAAi*-treated Al Mg1; (c) *SAAu*-treated Al Mg1.

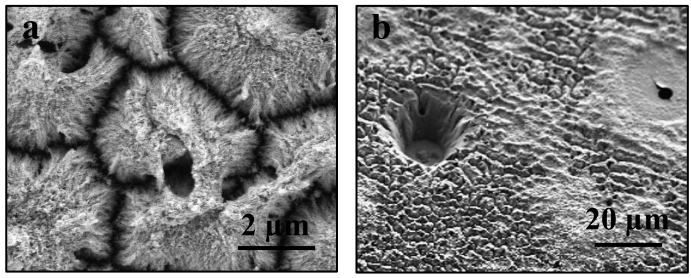

Figure 2. SEM images of specimen surfaces following a cathodic chitosan deposition on *SAAi*-treated surfaces; (a) Al Mg1, *SAAi* + *Chs-e*; (b) Al99.5, *SAAi* + chitosan deposition at higher pH, for larger current density and for longer duration.

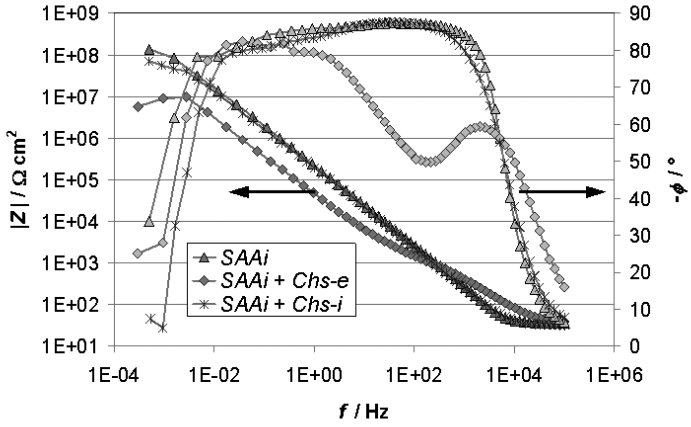

Figure 3. EIS spectra for *SAAi*, *SAAi* + *Chs-e* and *SAAi* + *Chs-i* in phosphate buffer; rod specimens; Bode plot: modulus of impedance, $|Z|$ and phase angle, ϕ *vs.* frequency, f.

hence, deprotonation of the previously produced polycations of the type R–NH_3^+ [11, 18]. For optimized process conditions, the organic material is homogeneously precipitated and practically cannot be seen in SEM micrographs (Fig. 2a). For too high solution pH, current density and duration, inhomogeneous precipitation occurs (Fig. 2b). Additionally, cone-like microscopic defects form, probably due to the concurrent hydrogen formation and bubble expansion at the metal–oxide interface.

EIS measurements indicated that defects were present independent of the actual manner of cathodic chitosan deposition. As Fig. 3 shows for the optimized *Chs-e* deposition conditions, the curve of the impedance modulus $\log|Z|$ *vs.* $\log f$ is markedly shifted to lower values for $f < 1$ kHz in comparison with the original anodized state *SAAi*. This observation is indicative of the formation of a more porous oxide structure. On the contrary, specimens that were merely immersed in chitosan solution (*SAAi* + *Chs-i*) gave practically the same impedance spectrum as *SAAi*. An analogous situation was found for *SAAu*-treated specimens.

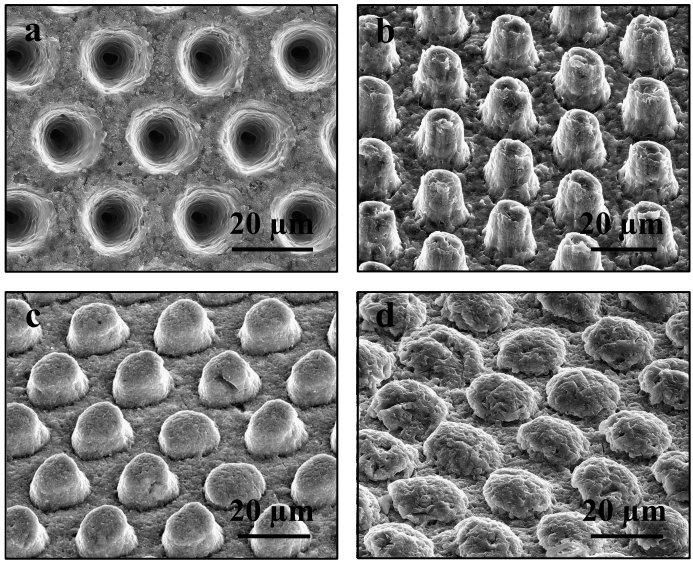

Figure 4. SEM images of the laser-structured SiC embossing die (a; top view) and of mechanically structured Al Mg1 surfaces (b–d; specimens tilted in SEM); (b) *ME*; (c) ME + MB (grit 1200); (d) ME + MB (grit 600).

As an alternative to the anodic route of micro-roughening, micro-embossing was employed at elevated temperatures. Figure 4a, b shows the SiC embossing die with its regular array of laser-formed cavities and the embossed Al Mg1 metal surface, respectively. The protrusions of the latter have a shape and arrangement which are very similar to patterns found on the lotus leaf. The die removal did not cause damage to either the metal nor to the tool. It should be noted that the hardness of Al Mg1 is relatively high. Therefore, it was necessary to employ an elevated-temperature embossing technique, in which both the tool and the sheet sample were heated. At ambient temperatures the pattern was not completely transferred. However, ambient-temperature embossing was found to be suitable for Al 99.5, which has about 2/3 of the hardness of Al Mg1.

An additional blasting treatment gave the surface a uniform roughness, but also caused abrasion and deformation of the protruding bumps. The latter was more pronounced for the rather coarse 600 grit powder compared with 1200 grit (Fig. 4c, d).

3.2. Coated Surfaces

The grafted hydrophobizing polymer *POMA* forms very thin f lms, comparable to the wet-deposited *PFATES* and *AS/TAF* coatings. Thus, the underlying micro-mountain-like morphology (Fig. 1b) is fully preserved in these cases.

For the *HFCVD*-generated *PTFE* layers, the microscopic shape is noticeably different, because of the inherent morphological properties of the deposits. The specifi morphology of the coating is more pronounced with increasing thickness (50–1000 nm) and, moreover, it is dependent on the deposition conditions employed.

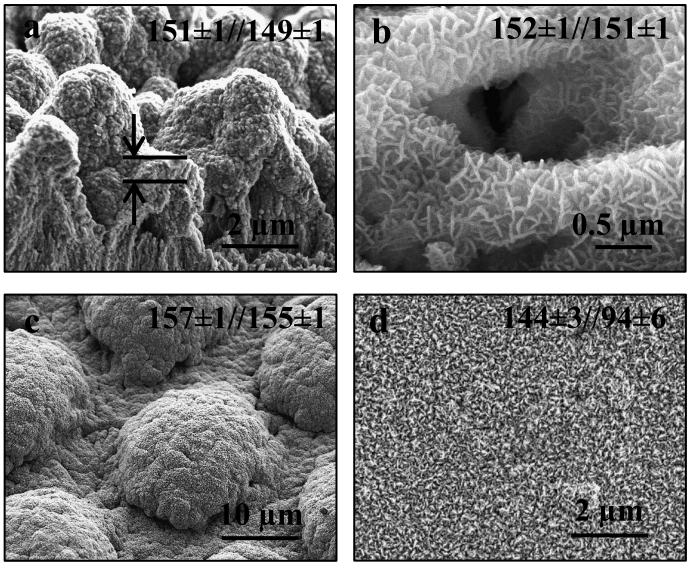

Figure 5. SEM images for different treatments and corresponding DCA data ($\theta_a//\theta_r$); (a) *SAAi*+*PTFE* (standard coating, 1000 nm), fractured specimen showing its outermost surface (upper part) and the fractured area (lower part), fractured *PTFE* layer marked by arrows; (b) *SAAi* + *PTFE* (annealing type 1, 500 nm); (c) *ME* + *MB* (grit 600) + *PTFE* (standard coating, 1000 nm); (d) Smooth metallic substrate + *PTFE* (standard coating, 1000 nm); (a–c: specimens tilted by 35°, d: top view, b: acceleration voltage 10 kV).

While the standard coating conditions produce a shape with very small protrusions of about 0.1 µm height (Fig. 5a, d), other deposition regimens produce interpenetrating f akes of 0.2–0.4 µm in diameter (Fig. 5b). The cryo-fractured sample of Fig. 5a shows that the *PTFE* layer follows the substrate's oxide surface profile where the new micro-profil is slightly more rounded than that of the oxide. The real coating thickness in the case of the micro-rough *SAAi* substrate can be derived likewise. Fig. 5c shows the situation for a standard-coated, *ME/MB*-pretreated substrate.

Nearly all the investigated combinations of roughening and coating treatments led to superhydrophobic properties with CAs of around 150° and a generally negligible hysteresis. The entire wetting results can be seen in Table 1. In Fig. 5a–d the corresponding DCA data are displayed. The data demonstrate that various roughening pretreatments have different impacts on the SH, in particular on the receding angles. In detail, SH is not preserved when i — *SAAi* is replaced by *SAAu*, ii — 600 blasting grit is replaced by 1200 grit, or iii — the micro-blasting step is completely omitted. These examples emphasize that a sufficien degree of roughness of the substrate is definitel necessary in order to achieve SH.

When there was no roughening pretreatment, as in the case of a mere *PTFE* standard coating on a smooth sheet (Fig. 5d), then the receding angle was dramatically reduced down to less than 100°. The advancing angle was also affected ($(144 \pm 3)°$). This means that the specifi morphology of thicker hydrophobic

Table 1.
Data compilation for the as-coated states and after the artificia weathering exposure (*WTH*); column 1: sequence of treatments (details, coating thickness) [number of specimens included]; columns 2 and 3: wetting properties according to DCA measurements stated as CA averages ± standard deviations for single specimens or CA spans for several specimens of the same type; column 4: carbon to fluorin elemental ratios acc. to XPS (single specimens)

Treatment	Contact angles (θ_a / ° // θ_r / °) (as coated)	Contact angles (θ_a / ° // θ_r / °) (after *WTH*)	c(F) / c(C) (before → after *WTH*)
SAAi + *Chs* + *POMA* [3]	153 // 152	superhydrophilic	–
SAAi + *PFATES* [2]	153 // 152	152–154 // 148–150	1.8 → 1.6
SAAi + *AS*/*TAF* [2]	152 // 151–152	154 // 151–152	1.4 → 1.7
SAAi + *PTFE* (std. coat., 250–1000 nm) [6]	151–152 // 148–151	142–153 // 130–147	2.1 → 1.9
SAAi + *Chs* + *PTFE* (std. coat., 250–1000 nm) [4]	151–152 // 149–151	133–150 // 99–130	–
SAAi + *PTFE* (annealing type 1, 500 nm) [2]	151–152 // 151	152 // 147–148	2.0 → 2.0
SAAi + *PTFE* (annealing type 2, 500 nm) [1]	153 ± 1 // 151 ± 1	152 ± 2 // 142 ± 2	2.1 → 2.1
SAAi + *PTFE* (elevated substrate temp., 500 nm) [1]	151 ± 1 // 150 ± 1	152 ± 1 // 150 ± 1	2.2 → 2.1
SAAi + *PTFE* (lower pressure, 500 nm) [1]	152 ± 1 // 151 ± 1	154 ± 1 // 141 ± 1	1.8 → 2.0
SAAu + *PTFE* (std. coat., 50–1000 nm) [3]	151–153 // 140–144	127–134 // 47–70	2.1 → 1.6
Pickled metallic substrate + *PTFE* (std. coat., 500 nm) [1]	153 ± 1 // 149 ± 1	137 ± 4 // 79 ± 2	–
Smooth metallic substrate + *PTFE* (std. coat., 1000 nm) [1]	144 ± 3 // 94 ± 6	112 ± 4 // 73 ± 11	–
ME + *PTFE* (std. coat., 1000 nm)	151 ± 3 // 147 ± 5	154 ± 1 // 149 ± 1	–
MB (grit 1200) + *PTFE* (std. coat., 1000 nm) [1]	151 ± 1 // 146 ± 2	127 ± 11 // 84 ± 27	–
ME + *MB* (grit 1200) + *PTFE* (std. coat., 1000 nm) [1]	151 ± 2 // 146 ± 2	150 ± 1 // 146 ± 3	–
MB (grit 600) + *PTFE* (std. coat., 1000 nm) [1]	157 ± 1 // 155 ± 1	151 ± 2 // 141 ± 7	–
ME + *MB* (grit 600) + *PTFE* (std. coat., 1000 nm) [1]	155 ± 1 // 153 ± 1	152 ± 1 // 146 ± 1	–

PTFE coatings is insuff cient to achieve superhydrophobic properties. On the other hand, the advancing angle is markedly higher than the value of 108° stated for smooth *PTFE* material [21].

EIS measurements yielded results for *SAAu* + *PTFE* (standard coating) specimens that were quite similar to different wet-deposited, thin-fil coatings [22]. Increasing *PTFE* thickness leads to higher impedance levels of the 'plateaus' at intermediate frequencies in the $\log|Z| - \log f$ curves (Fig. 6). However, the resistance of the anodic barrier layer, expressed by the impedance level in the sub-mHz region, is the largest in the entire system. Measurements on *SAAi*-based sheet spec-

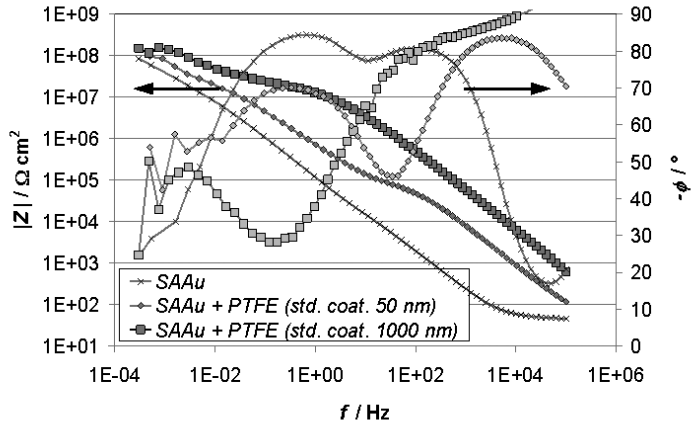

Figure 6. EIS spectra for *SAAu*, *SAAu* + *PTFE* (std. coat., 50 nm), and *SAAu* + *PTFE* (std. coat., 1000 nm) in phosphate buffer; sheet specimens; Bode plot: modulus of impedance, $|Z|$ and phase angle, ϕ *vs.* frequency, f.

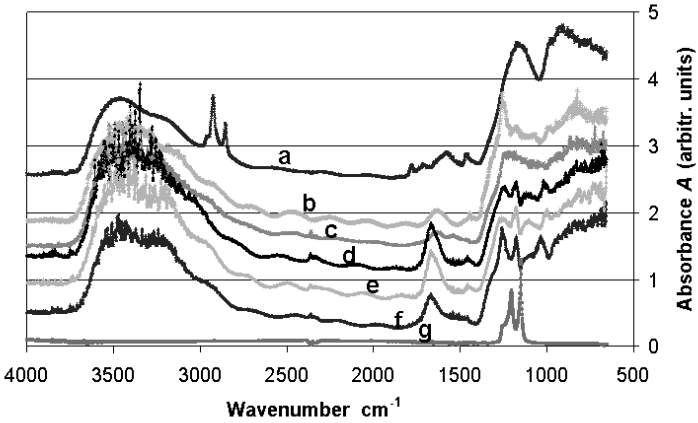

Figure 7. FT–IRRAS absorbance spectra for different samples; (a) *SAAi* + *Chs-e* + *POMA*; (b) *SAAi* + *PFATES*; (c) *SAAi* + *AS/TAF*; (d) *SAAi* + *PTFE* (std. coat., 500 nm); (e) *SAAi* + *PTFE* (annealing type 1, 500 nm); (f) *SAAi* + *PTFE* (lower pressure deposition, 500 nm); (g) *MB* + *PTFE* (std. coat., 1000 nm).

imens could not be satisfactorily made because of an inconsistent effective area during immersion due to capillary effects.

The chemical properties of the coating–substrate systems were investigated by means of FT–IRRAS and XPS. The infrared spectra were highly reproducible for a particular sample so that only one spectrum for each is displayed in Fig. 7. The *POMA*-modifie surface showed C–H stretch bands at 2851 and 2923 cm^{-1} (Fig. 7, curve a) indicating the presence of long alkyl chains, which are responsible for diminished surface free energy. The presence of C–O and C=O bonds is indicated by the small bands at 1700–1770 cm^{-1}. For the F-containing coating compounds the typical C–F stretch vibrations were recorded most clearly with

PTFE coating on *ME/MB* substrates (Fig. 7, curve g). The two bands at 1150 and 1205 cm^{-1} (shoulder at 1260 cm^{-1}) are in agreement with literature data [19, 20]. For *SAAi*-pretreated specimens the positions of these bands deviate significantl . Additionally, the absorbance pattern in this region slightly varies for the different *PTFE* types (Fig. 7, curves d–f), where the coating generated at lower pressure shows a small deviation. When the thickness of the standard coating is varied, the band at about 1175 cm^{-1} remains constant in contrast to the band beyond 1200 cm^{-1}, which undergoes a shift. This results from a superposition with a band resulting from the oxide substrate.

For the application of XPS to specimens with a *rough* surface it should be noted that the real take-off angles, and, hence the information depth, vary locally. This is especially true for *SAAi*-based samples with their steep micro-profile According to the f ndings, the C_{1s} high resolution spectra reveal a more or less complex structure, which results from the respective structure and binding situations of the different coating compounds analyzed. For the thin wet-deposited *Chs* + *POMA* coating the C_{1s} spectrum of the composite layer (Fig. 8b) shows a dominant component peak (*A*) which is mainly due to *POMA's* octadecyl groups. The two component peaks *C* and *D*, which are typical for the C–O–(H, C) and O–C–O (acetal) groups of chitosan (Fig. 8a), respectively, are strongly diminished. This indicates that the chitosan layer is completely covered by *POMA*. Amide and imide groups, formed during the reaction between chitosan and *POMA*, were identifie as the cause of the component peaks *E* and *G* [23]. The situation is similarly complex for the cases of *PFATES* and *AS/TAF* (Fig. 8c, d). The fluorosilan *PFATES* contains groups such as $–CH_2–$, $–CF_2–$ and $–CF_3$, whereas the carbon atoms of the duplex fil *AS/TAF* are bound to the hetero elements silicon, nitrogen, oxygen (C–O–C), and fluorin ($–CF_2–$, $–CF_3$). The C–F bonds are characterized by high binding energies $E_b \geqslant 292$ eV; they correspond to the component peaks *Y* and *Z*. It should be noted that in the cases of thin coatings the measured high oxygen contents of about 30 at.% do not come from the coatings alone, but also from the oxidized Al oxide. This is confirme by the detection of Al (ca. 9 at.%).

For specimens with different 500 nm thick *PTFE* coatings the F/C ratios were higher than in the cases of the F-containing wet-deposited coatings (Table 1). The ratios were in the range 1.8–2.2, i.e. near the theoretical value for *PTFE*. In the case of bulk *PTFE* material a ratio of 2.1 was determined. Most of the C_{1s} spectra are dominated by the peak at 292 eV, which is attributable to the $–CF_2–$ units in the polymer chains (Fig. 8e). The lower pressure coating variant is characterized by a considerably higher proportion of $–CF_3$ bonds (Fig. 8f). Moreover, there is a noticeable contribution of carbon with a lower binding energy. This is consistent with the considerable oxygen content of about 13 at.% (it generally does not exceed 2 at.%). These finding indicate that the lower pressure formation conditions result in marked deviations from the regular *PTFE* composition. It is expected that the compound trifluoroacety fluorid CF_3CFO, which is one of the products formed

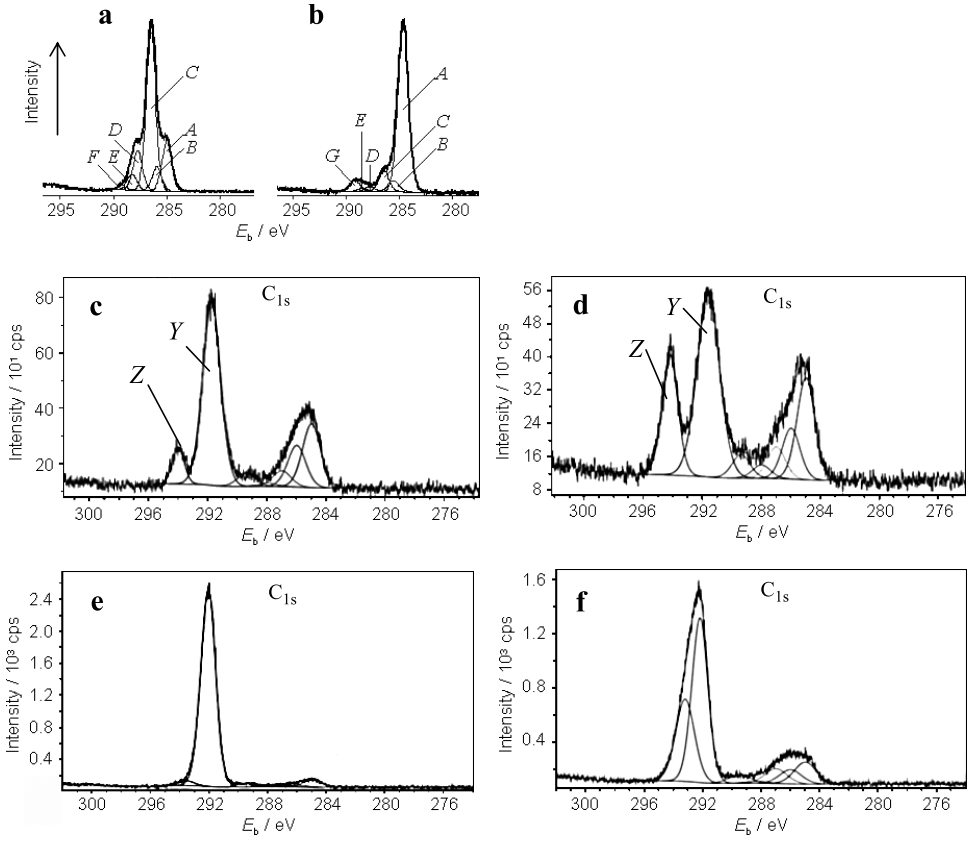

Figure 8. C_{1s} high-resolution ×*PS* spectra of *SAAi*-based specimens with different coatings; (a) *SAAi* + *Chs*; (b) *SAAi* + *Chs* + *POMA*; (c) *SAAi* + *PFATES*; (d) *SAAi* + *AS/TAF*; (e) *SAAi* + *PTFE* (std. coat., 500 nm); (f) *SAAi* + *PTFE* (lower pressure deposition, 500 nm).

by the thermal decomposition of hexafluoropro ylene oxide [20], still plays a role in this type of polymer coating.

3.3. Coated Surfaces Followed by Artificia Weathering

After having undergone the *WTH* exposure, the specimens revealed no visual alterations. Moreover, the SEM examination showed practically unchanged morphological properties.

The wetting behavior of the exposed samples, however, gave a different picture. As the CA data clearly document (Table 1, third column), degradation phenomena were observed, the degree of which was influence by the respective treatments:

i — Practically no changes in the CAs were observed for *PFATES*, *AS/TAF*, *PTFE* (annealing type 1), and *PTFE* (elevated substrate temperature), all on *SAAi* substrates. The same finding are true also for *ME* + *PTFE* (std. coat.), and *ME* + *MB* (different grit sizes) + *PTFE* (std. coat.).

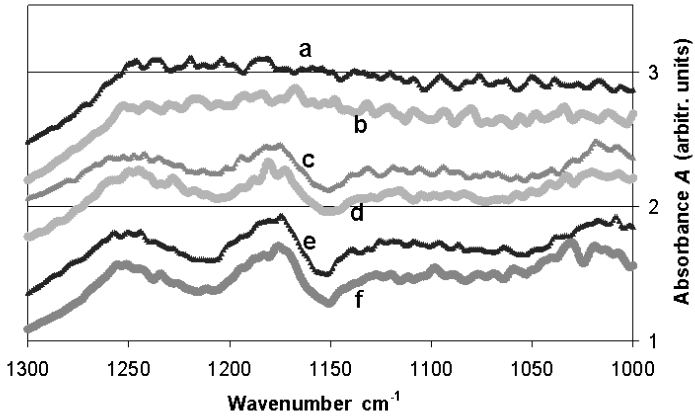

Figure 9. FT–IRRAS absorbance spectra for different samples before and after artificia weathering; (a, b) *SAAi* + *AS/TAF* + *WTH* (for b); (c, d) *SAAi* + *PTFE* (std. coat., 500 nm) + *WTH* (for d); (e, f) *SAAi* + *PTFE* (elevated substrate temperature, 500 nm) + *WTH* (for f).

ii — Moderate changes in the wetting behaviour with receding angles of about 140° were observed for *SAAi* + *PTFE* (std. coat., annealing type 2 and lower pressure coating), and *MB*-600 + *PTFE* (std. coat.). Here, the advancing angles still remained at the SH level.

iii — Considerable worsening occurred with *SAAi* + *Chs-e* + *PTFE* (std. coat.), where also the advancing angle decreased.

iv — A dramatically worsened behavior was observed for *SAAi* + *Chs* + *POMA* (becoming completely hydrophilic), *SAAu* + *PTFE* (std. coat.), pickled substrate + *PTFE* (std. coat.), smooth metal + *PTFE* (std. coat.), and *MB* (grit 1200) + *PTFE* (std. coat.).

It follows from the DCA measurements that the behavior after the *WTH* exposure of the specimens with a *PTFE* standard coating was noticeably variable in spite of the same initial surface chemistry. Specimens with only low roughness appear to undergo a more pronounced SH degradation during *WTH* compared to the rougher specimens. The reason is not yet clear.

An attempt was made to relate the actual wetting properties and their changes to the corresponding surface chemistry f ndings. FT–IRRAS revealed that the C–F-related region at 1150–1200 cm^{-1} was not influence by *WTH* as seen from the spectra in Fig. 9 for different layer systems, despite the *different* impact of exposure on their wetting behavior. However, the content of water in all the specimen types was slightly higher than before the exposure.

XPS is known to be more sensitive to changes in the outermost surface, which governs the wetting behavior. For *SAAi*-based specimens covered with *PFATES* or *AS/TAF*, where there were no significan changes in the wetting properties following *WTH*, interesting features were detected by XPS. In the case of *PFATES*, the finding reveal a very high stability of this coating compound under the conditions of the exposure (Table 1, Fig. 10a, b). However, for the *AS/TAF* coating, an *increase*

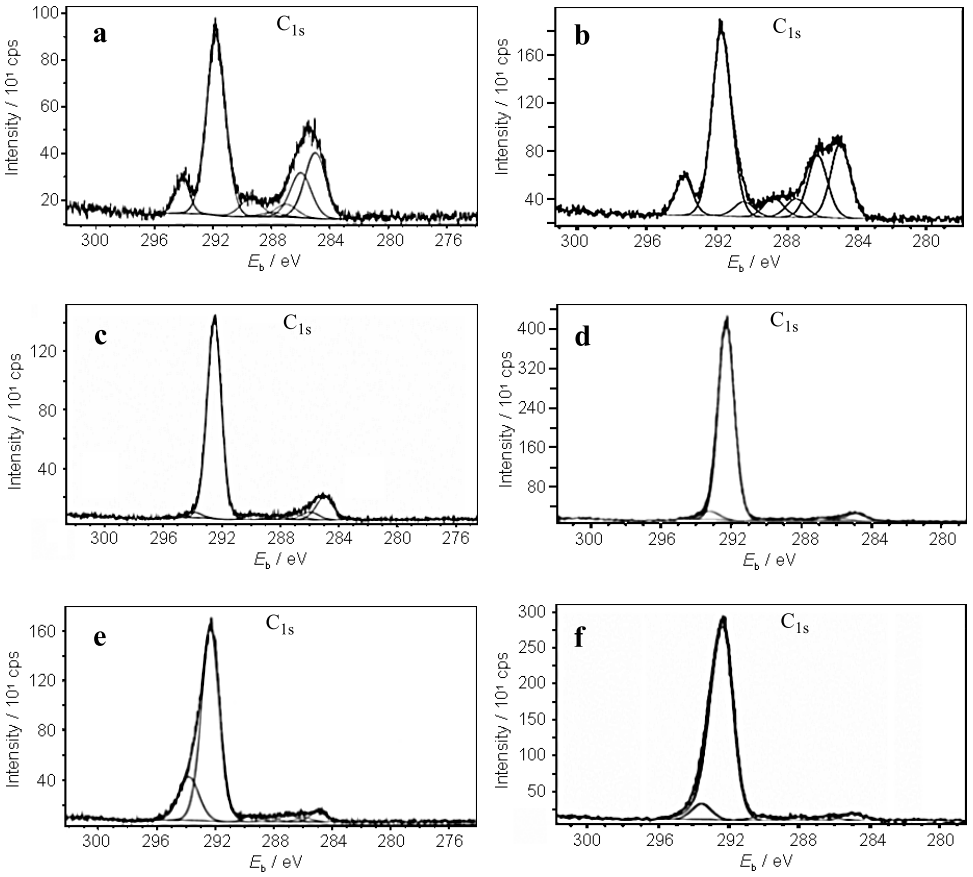

Figure 10. C_{1s} high-resolution $\times PS$ spectra for artificiall weathered, *SAAi*-based specimens with different coatings; (a, b) *SAAi* + *PFATES* + *WTH* (for a) or + *WTH-L* (for b); (c, d) *SAAi* + *PTFE* (std. coat., 500 nm) + *WTH* (for c) or + *WTH-L* (for d); (e, f) *SAAi* + *PTFE* (enhanced substrate temperature, 500 nm) + *WTH* (for e) or + *WTH-L* (for f).

in the F/C ratio was accompanied by a *decrease* of the low-energy components of the carbon signal, whereas the F-bound carbon signal remained at a high level. This shows that the primary aminosilane coating component, which is free of f uorine, underwent vast degradation in the course of the exposure.

For *PTFE* standard coatings the weathering impact was found to be generally higher according to the XPS measurements. As mentioned above, at least some of the *SAAi*-based specimens underwent noticeable drops in the receding angles (Table 1) such that SH was not fully preserved in these cases. Figure 10c indicates, for a *SAAi* + *PTFE* (std. coat.) specimen, that the proportion of electropositively bound carbon (low binding energy) has increased as a result of the *WTH* exposure (cf. Fig. 8e). This findin is associated with an increase in the oxygen content, which represents some newly generated side groups or breaking of the polymer backbone.

For *SAAi* + *PTFE* (elevated substrate temperature) + *WTH*, which was found to preserve very high CAs, XPS measurements indicated that the proportion of electropositively bound carbon remained lower than for the standard coating type *PTFE* (Fig. 10c, e). Thus, XPS was found to be a valuable tool in relating the wetting behavior with the elemental composition of the uppermost surface layer.

An additional weathering experiment excluded moisture so that only a dry light irradiation took place over 360 h (*WTH-L*). The advancing contact angles were found to be nearly the same as measured after the regular *WTH* procedure, but the receding CAs were drastically diminished and, generally, showed a higher scatter. In the best case, values of $(150 \pm 3)°//(119 \pm 10)°$ were obtained for *SAAi* + *PTFE* (elevated substrate temperature, 500 nm) after *WTH-L*. Despite these findings, the C_{1s} high resolution spectra for the *PTFE*-coated specimens were generally very similar to those after regular *WTH* (exposure cf. spectra pairs of Fig. 10). These findings suggest that the various coating compounds might have been affected by the dry exposure in different ways and that the damaging mechanism without moisture may be different from that for regular *WTH* conditions, where the water is expected to influence the actual degradation. In light of the XPS findings the worsened wetting properties (especially lowered θ_r) after *WHT-L* might be explained by small local coating defects, which are responsible for local pinning during the receding of the wetting triple line in the course of the dynamic CA measurement.

4. Conclusions

In order to investigate the effects of preparation differences on superhydrophobicity (SH) and to judge the weathering stability, a variety of roughening pretreatments (electrochemical and mechanical) and water-repellent coatings (wet-deposited thin film and *PTFE* film generated by hot-filament chemical vapor deposition) were considered and tested. The chemical stability was investigated by employing a standardized artificial weathering test.

Within the experimental conditions, noticeable influences on the wetting properties of the coated systems were found to depend on the manner of roughening. Superhydrophobicity was achieved in those cases, where the pretreatment generated a suitable degree of sub-micro-roughness and micro-roughness components, e.g. with the anodization route *SAAi* or for micro-embossed plus micro-blasted surfaces. The usual anodization *SAAu* and mere etching caused worsened water-repellent properties, although there was a contribution from the inherent micro-roughness of the *HFCVD*-produced *PTFE* films

For artificial weathering exposure, a very high stability of superhydrophobicity was observed for the fluorinated wet-deposited *PFATES* and *AS/TAF* coatings as well as for *PTFE* deposited at an elevated substrate temperature, all on *SAAi*-pretreated substrates. Very good results were also obtained for specimens produced by appropriate mechanical roughening in combination with *PTFE* coatings. As a rule, deteriorating water-repellent properties were associated with a decrease in the

XPS-derived fluorine concentration and the F/C ratio as well as with an increase of the oxygen concentration. The *AS/TAF* duplex fil underwent decomposition of the aminosilane component as a result of the weathering. The weathering stability of the *PTFE* standard coating was found to be better on the *SAAi* substrates as compared to those treated by *SAAu* or etching.

Acknowledgements

This work was, partly, supported by a grant from the Saxon State Ministry of Science and Fine Arts (Saechsisches Staatsministerium fuer Wissenschaft und Kunst, SMWK). One of us (A.P.) appreciates the support of the German Academic Exchange Service (DAAD). The micro-embossing and micro-blasting methods were developed by Mr. T. Burkhardt and Mr. J. Engelmann (FhG-IWU Chemnitz). The experimental contributions of Mrs. K. Galle (TUD) and Mrs. B. Schneider (IPF) are also greatly acknowledged.

References

1. W. Barthlott and C. Neinhuis, *Planta* **202**, 1–8 (1997).
2. D. Öner and T. J. McCarthy, *Langmuir* **16** (20), 7777–7782 (2000).
3. Y. Yu, Z.-H. Zhao and Q.-S. Zheng, *Langmuir* **23**, 8212–8216 (2007).
4. M. Nosonovsky and B. Bhushan, *Ultramicroscopy* **107**, 969–979 (2007).
5. S. Shibuichi, T. Yamamoto, T. Onda and K. Tsujii, *J. Colloid Interface Sci.* **208**, 287–294 (1998).
6. W. A. Zisman, in: *Contact Angle, Wettability and Adhesion*, Adv. Chem. Ser. No. 43, pp. 1–51. American Chemical Society, Washington, DC (1964).
7. M. Pagliaro and R. Ciriminna, *J. Mater. Chem.* **15**, 4981–4991 (2005).
8. M. Callies and D. Quéré, *Soft Matter* **1**, 55–61 (2005).
9. M. Ma and R. M. Hill, *Current Opinion Colloid Interface Sci.* **11**, 193–202 (2006).
10. J. Wang, Y. Yu and D. Chen, *Chinese Science Bulletin* **51**, 2297–2300 (2006).
11. C. Blank, M. Thieme, V. Hein, H. Worch, T. Burkhardt, R. Frenzel, S. Höhne, H. Pryce Lewis and A. J. White, in: *Aluminium Alloys — Their Physical and Mechanical Properties*, J. Hirsch, B. Skrotzki and G. Gottstein (Eds), pp. 2131–2138. Wiley-VCH, Weinheim (2008).
12. R. Wang, K. Hashimoto and A. Fujishima, *Nature* **388**, 431–432 (1997).
13. M. Thieme, R. Frenzel, S. Schmidt, H. Worch, F. Simon and K. Lunkwitz, *Adv. Eng. Mater.* **3**, 691–695 (2001).
14. M. Thieme, R. Frenzel, V. Hein and H. Worch, *J. Corrosion Sci. Eng.* **6**, Paper 47 (2003).
15. R. Frenzel, S. Schmidt, V. Hein, M. Thieme and F. Simon, in: *Verbundwerkstoffe*, H. P. Degischer (Ed.), pp. 489–493. Wiley-VCH, Weinheim (2003).
16. C. Blank, R. Frenzel, V. Hein, B. Schmidt, F. Simon, M. Thieme, K. Tittes and H. Worch, in: *Praktische Metallographie, Sonderband*, Vol. 36, G. Petzow (Ed.), pp. 491–496. Werkstoffinfo - mationsges, Frankfurt (2004).
17. K. Tittes, B. Schmidt, C. Blank, V. Hein, H. Worch, F. Simon and R. Frenzel, in: *GdCh-Monographie*, Vol. 32, J. Besenhard and J. Russow (Eds), pp. 176–184. GdCh, Frankfurt (2004).
18. C. Blank, V. Hein, M. Thieme, H. Worch, S. Höhne and F. Simon, in: *Praktische Metallographie, Sonderband*, Vol. 39, G. Petzow (Ed.), pp. 175–182. Werkstoffinformationsges Frankfurt (2007);

C. Blank, S. Höhne, M. Thieme, H. Worch, R. Frenzel, F. Simon and V. Hein, Pending patent application at Deutsches Patent- und Markenamt, Munich, 11.09.2007.
19. K. K. S. Lau, J. A. Caulfiel and K. K. Gleason, *Chem. Mater.* **12**, 3032–3037 (2000).
20. K. K. S. Lau, S. K. Murthy, H. G. P. Lewis, J. A. Caulfiel and K. K. Gleason, *J. Fluorine Chem.* **122**, 93–96 (2003).
21. K. K. S. Lau, J. Bico, K. B. K. Teo, M. Chhowalla, G. A. J. Amaratunga, W. I. Milne, G. H. McKinley and K. K. Gleason, *Nano Lett.* **3**, 1701–1705 (2003).
22. M. Thieme and H. Worch, *J. Solid State Electrochem.* **10**, 737–745 (2006).
23. S. Höhne, R. Frenzel, A. Heppe and F. Simon, *Biomacromolecules* **8**, 2051–2058 (2007).
24. D. Briggs, *Characterization of Surfaces*. Pergamon, Oxford (1989).
25. M. P. Seah and W. A. Dench, *Surface Interface Anal.* **1**, 2 (1979).
26. G. Beamson and D. Briggs, *High Resolution XPS of Organic Polymers*, The Scienta ESCA 300 Database. Wiley, Chichester (1992).